telecom

MDPI

Article

An Automated GA-HSMLFMM Co-Design Framework for Minimizing DDM in ILS Multipath Interference

Zihao Li [1], Jiarong Lin [1], Zexin Lin [1], Lixiang Zuo [1], Mingjia Wang [2] and Liyun Zuo [3,*]

[1] School of Information Engineering, Guangdong Polytechnic, Foshan 528041, China; lizihao1@gdpt.edu.cn (Z.L.); linjiarong1@gdpt.edu.cn (J.L.); linzexin@gdpt.edu.cn (Z.L.); zuolixiang@gdpt.edu.cn (L.Z.)
[2] Technical Support Center, Middle South Regional Air Traffic Management Bureau, Guangzhou 510000, China; znjibaohr@atmb.net.cn
[3] School of Computer Science, Guangdong University of Petrochemical Technology, Maoming 525000, China
* Correspondence: zuoliyun@gdupt.edu.cn

Abstract

To ensure the guidance accuracy and flight safety of instrument landing systems (ILSs), it is imperative to mitigate multipath interference caused by reflections from airport structures, whose core detrimental effect is the excess deviation of the difference in depth of modulation (DDM). This paper presents an automated design methodology with the explicit objective of directly minimizing DDM, employing a genetic algorithm (GA) to optimize additional metallic baffles adjacent to a building, thereby achieving a "stealth" effect for the building structure. The method encodes the layout parameters of additional metallic baffles adjacent to a building into chromosomes, searching for the optimal configuration through iterative evolution. Each generation applies the efficient half-space multilevel fast multipole method (HSMLFMM)—for the first time in ILS interference simulation—to accurately compute the radiation field of every candidate design. The maximum resultant DDM along the glide path serves as the fitness function for selection. Optimization and validation are conducted for four typical scenarios where the interference source is located 50, 100, 150, and 200 m from the runway centerline. The optimized DDM values are reduced to 4.49, 4.78, 4.63, and 4.87, respectively, all below the ICAO Annex 10 tolerance limit of 5μAfor CAT III operations. The corresponding reduction percentages are 75.85%, 83.93%, 90.73%, and 90.19%, with a maximum reduction of 90.73% achieved in the 150 m scenario. This research establishes an efficient, automated closed-loop optimization workflow, which offers a viable approach for the intelligent and precision design of low-observable buildings at airports.

Keywords: instrument landing system; multipath interference; difference in depth of modulation; genetic algorithm; stealth structures; half-space multilevel fast multipole method

Check for updates

Academic Editor: Achilles Boursianis

Received: 4 April 2026
Revised: 22 June 2026
Accepted: 1 July 2026
Published: 3 August 2026

Copyright: © 2026 by the authors. Licensee MDPI, Basel, Switzerland. This article is an open access article distributed under the terms and conditions of the Creative Commons Attribution (CC BY) license.

1. Introduction

The instrument landing system (ILS), an indispensable ground-based precision approach and landing guidance system in civil aviation, has a signal reliability that directly impacts flight safety. Within this system, the localizer (LOC) and glide path (GP) beacons, respectively, provide horizontal and vertical guidance information for aircraft during approach [1]. However, with the rapid expansion of air transport, the proliferation of structures near airports—including high-rise buildings, hangars, and control towers—has intensified the challenge of multipath interference (reflection, refraction, and scattering)

affecting ILS signals. Such interference distorts the radiation pattern of the localizer, compromising the accuracy of the difference in depth of modulation (DDM) and thereby posing potential threats to flight safety [2].

To mitigate multipath interference, Thain et al. proposed a solution termed "stealth buildings" [3]. This approach employs specially designed structures around airports to attenuate multipath effects. However, this method demands considerable expertise from designers, and the unique shapes and positions of different buildings make such design experience difficult to generalize. Consequently, tailored designs addressing the specific obstacle distributions at different airports are essential.

Heuristic algorithms play a significant role in stealth platform design. These algorithms can search for optimal design paths tailored to specific optimization objectives, with results potentially surpassing traditional design methods. Zhao et al. employed heuristic algorithms for stealth material design [4], Xing et al. utilized them for stealth antenna design [5], and Ren et al. applied them to design intelligent metasurfaces to reduce antenna radar cross-sections [6]. Inspired by these approaches, heuristic algorithms may also be applied to the design of stealth structures.

Common heuristic algorithms include genetic algorithms (GAs) [7], differential evolution (DE) [8], and particle swarm optimization (PSO) [9]. Among these, genetic algorithms are widely employed due to their strong capability to search for optimal solutions. Cheng et al. [10] employed a genetic algorithm to design a broadband decoupling and matching network (DMN) for a two-element antenna array. Wang et al. [11] utilized a competitive and cooperative approach, combining GA with an inverse neural network (INN) for the design of a dielectric lens antenna. Gao et al. [12] introduced a hybrid algorithm (SADE-SBLO) that integrates a self-adaptive differential evolution (SADE) with a simplified Bayesian local optimizer (SBLO) to enhance the efficiency of antenna optimization. Ha et al. [13] employed machine learning-assisted DE for multi-band antenna design. Wan et al. [14] utilized a hybrid GA-PSO approach to design a single-plane quasi-isotropic folded dipole. Bagherkhani et al. [15] introduced a novel adaptive solution space method incorporating PSO, applying it to microstrip antenna design.

Given the substantial number of iterations typically required in genetic algorithms, a computationally efficient yet accurate electromagnetic simulation algorithm must be integrated into the optimization loop for performance evaluation. This work bridges this gap by, for the first time, applying the half-space multilevel fast multipole method (HSMLFMM) [16] to the high-fidelity simulation of ILS multipath interference scenarios. To justify the unique suitability of HSMLFMM for this optimization task, a comparison with mainstream existing simulation methods is necessary. Common methods for instrument landing system signal simulation include ray tracing (RT) [17], the multilevel fast multipole method (MLFMM) [18], the method of moments (MoM) [19], and the finite-difference time-domain (FDTD) method [20]. While ray tracing is computationally efficient, its limited accuracy, based on high-frequency approximations, hinders its application to the precise simulation of complex near-field scattering essential for DDM calculation. On the other hand, FDTD and MoM achieve high accuracy at the expense of considerable computational overhead, making them prohibitive for an optimization process requiring thousands of simulations. The conventional full-space MLFMM, while suitable for large-scale scattering problems, requires meshing the entire ground plane when modeling ILS scenarios near the airport surface, introducing a significant and unnecessary computational burden.

In contrast, the HSMLFMM leverages a half-space Green's function that inherently satisfies the boundary conditions of a ground plane medium. This fundamental advantage eliminates the need for ground surface meshing entirely, leading to substantial reductions in computational memory and time for simulations involving obstacles above ground

while preserving full-wave accuracy. Therefore, this work adopts the HSMLFMM as the electromagnetic simulation engine within the GA framework, establishing an efficient and precise evaluation loop that is uniquely suited for the automated optimization of ILS stealth structures.

The remainder of this paper is organized as follows. Section 2 elaborates on the working principle of the ILS and the proposed optimization framework that integrates the GA with the HSMLFMM, including the design of the fitness function and the genetic operators. Section 3 presents the experimental optimization results for different lateral distances (50 m, 100 m, 150 m and 200 m) and validates the effectiveness of the proposed method by the reduction percentage of the peak DDM. Section 4 summarizes the main work of this paper and discusses the limitations and future research directions.

The main contributions of this paper are summarized as follows:

(1) Proposing an automated GA-HSMLFMM co-design framework that directly minimizes DDM for ILS multipath interference mitigation, marking a paradigm shift from traditional "interference reduction" approaches to "direct DDM optimization."
(2) Incorporating HSMLFMM into the optimization loop for the first time, which inherently satisfies ground boundary conditions and eliminates the need for ground surface meshing, thereby substantially reducing computational overhead while preserving full-wave accuracy.
(3) Encoding metallic baffle layout parameters into GA chromosomes and establishing maximum resultant DDM along the glide path as the fitness function, enabling automated search for optimal stealth structure configurations.
(4) Validating the proposed framework across typical scenarios where interference sources are located 50 to 200 m from the runway centerline, demonstrating that the optimized stealth structures can reduce peak DDM by up to 90.73% and consistently converge below specified tolerance limits.

2. Overview of Theory and Formulation

2.1. ILSFundamentals

The ILS serves as a critical ground-based navigation aid, supplying both vertical and lateral guidance data to aircraft on final approach. The component responsible for azimuth guidance, the localizer, generates a directional radiation pattern through a horizontally configured antenna array.

As labeled in Figure 1, the localizer antenna is located on the runway centerline, radiating a carrier signal modulated by 90 Hz and 150 Hz tones. The left lobe (90 Hz dominant) and the right lobe (150 Hz dominant) are indicated by two blue ellipses. An approaching aircraft is shown to the left of the runway centerline. When the aircraft deviates to the left, it receives a stronger 90 Hz signal; when it deviates to the right, the 150 Hz signal dominates. The angle ϕ denotes the glide path elevation angle. The direct signal path from the antenna to the aircraft is drawn as a solid black line. To represent multipath interference, the figure also includes a stationary aircraft parked at a taxi position. The incident ray from the antenna hits the stationary aircraft and then reflects toward the approaching aircraft. The paths of this multipath propagation are marked as r_1 and r_2, with arrowheads indicating the direction of propagation.

With this configuration, the system operates on a carrier frequency of approximately 110 MHz by amplitude modulation (AM). The antenna is fed such that the signal is distributed to a central antenna and to two groups on either side, with specific phase differences (typically $\pm 90^\circ$) applied. This produces two primary radiation lobes slightly offset from the runway centerline, each identifiable by its unique modulation frequency. The core guidance parameter is the DDM, which is derived from the relative strengths of these

two lobes (as can be seen in Figure 2). The magnitude of the DDM is a direct function of the aircraft's horizontal deviation angle (ϕ) from the intended approach path. The minimum absolute DDM value typically occurs at the runway centerline. In ideal open terrain, the DDM on the glide path remains zero.

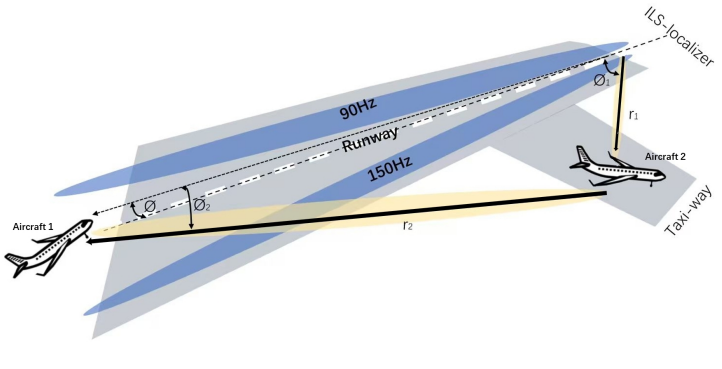


Figure 1. Sketch of ILS localizer function principle.

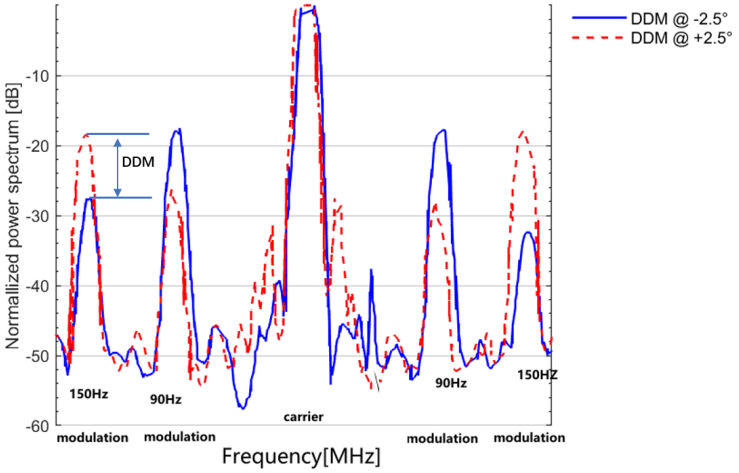


Figure 2. Measured spectrum example of an ILS localizer.

DDM is expressed in the form of the following equation:

$$DDM = \frac{2\boldsymbol{E}_{SBO}}{\boldsymbol{E}_{CSB}}\cos\phi \tag{1}$$

where $\boldsymbol{E}_{CSB}$ and $\boldsymbol{E}_{SBO}$ are the electronic amplitude of the carrier and sideband signal (CSB) and sideband-only signal (SBO), respectively, and ϕ is the angle between CSB and SBO.

International standards, governed by organizations such as ICAO, establish strict tolerance limits across three categories of operation (CAT I, II, and III), with CAT III being the most stringent. These tolerances for an ideal approach are depicted in Figure 3.

One notable threat to the reliability of the ILS guidance signal is the issue of multipath interference. Reflections of the localizer's signal from large objects on the ground, such as taxiing aircraft, can distort the intended radiation pattern. These reflected waves combine with the direct signal, potentially causing erroneous DDM values that exceed the permitted tolerances, thereby misleading the aircraft's navigation system. This article focuses on the interference caused by reflections from buildings near the airport.

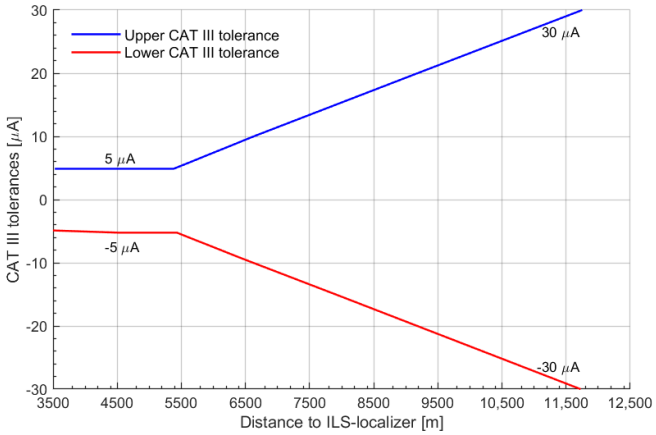


Figure 3. Allowed tolerances for ILS operation.

2.2. Integrated GA and HSMLFMM Optimization Method

2.2.1. Half-Space MLFMM Method

Three-dimensional obstacle scattering simulation can be modeled by combined field integral equations (CFIEs). In CFIE, the scattered electric field and magnetic field $\boldsymbol{E}^s$ and $\boldsymbol{H}^s$ and incident electric and magnetic field $\boldsymbol{E}^i$ and $\boldsymbol{H}^i$ can be modeled as:

$$\begin{aligned} \hat{t} \cdot [\gamma \boldsymbol{E}^i(\boldsymbol{r}) + \eta_i(1-\gamma)\hat{n} \times \boldsymbol{H}^i(\boldsymbol{r})] = \\ \hat{t} \cdot [-\gamma \boldsymbol{E}^s(\boldsymbol{r}) + \eta_i(1-\gamma)\boldsymbol{J}(\boldsymbol{r}) - \\ \eta_i(1-\gamma)\hat{n} \times \boldsymbol{H}^s(\boldsymbol{r})](\boldsymbol{r} \in S^+) \end{aligned} \tag{2}$$

where:

$$\boldsymbol{H}^s(\boldsymbol{r}) = \nabla \times \iint_{S'} \overline{\overline{G}}_{Aii}(\boldsymbol{r}, \boldsymbol{r}') \cdot \boldsymbol{J}(\boldsymbol{r}') dS' \tag{3}$$

where $\hat{n}$ and $\hat{t}$ are perpendicular and tangential vectors of the surface, respectively. $\boldsymbol{r} \in S^+$ is an infinitesimal distance outside the target surface. ϵ_i , μ_i and k_i are the permittivity, permeability and wavenumber of the target point. $\overline{\overline{G}}_{Aii}$ is the Green function. γ is the weighting factor (also known as the coupling parameter) that balances the electric field integral equation (EFIE) and magnetic field integral equation (MFIE) components in the combined field integral equation (CFIE), with $0 \leq \gamma \leq 1$. $\eta_i = \sqrt{\mu_i/\epsilon_i}$ is the intrinsic impedance of the medium. The obstacles are located at the upper half-space ($i = 1$, the image obstacles are located at $i = 2$ space). The unknown surface current $\boldsymbol{J}$ can be calculated by a set of N basis functions: $\boldsymbol{a}_{n'}$:

$$\boldsymbol{J}(\boldsymbol{r}') = \sum_{n'=1}^{N} I_{n'} \boldsymbol{a}_{n'}(\boldsymbol{r}') \tag{4}$$

To solve Equation (2), the Rao–Wilton–Glisson (RWG) basis function of MoM with a set of weighting functions $\boldsymbol{\omega}_n$ tangential to the target surface results in N linear equations for the unknown coefficients $I_{n'}$:

$$\boldsymbol{Z} \cdot \boldsymbol{I} = \boldsymbol{V} \tag{5}$$

where:

$$V_n = \iint_S \boldsymbol{\omega}_n(\boldsymbol{r}) \cdot [\gamma \boldsymbol{E}^i(\boldsymbol{r}) + \eta_i(1-\gamma)\hat{n} \times \boldsymbol{H}^i(\boldsymbol{r})] dS \tag{6}$$

$$\begin{aligned} Z_{nn'} = \gamma j\omega\mu_i \iint_S \iint_{S'} \boldsymbol{\omega}_n(\boldsymbol{r}) \cdot [\bar{\bar{I}} + \\ \frac{\nabla\nabla}{k_i^2}] \cdot \bar{\bar{\bar{G}}}_{Aii}(\boldsymbol{r}, \boldsymbol{r}') \cdot \boldsymbol{a}_{n'} dS' dS + \\ \eta_i(1-\gamma) \iint_S \boldsymbol{\omega}_n(\boldsymbol{r}) \cdot [\boldsymbol{a}_{n'}(\boldsymbol{r}) - \\ \hat{n} \times \nabla \times \iint_{S'} \bar{\bar{\bar{G}}}_{Aii}(\boldsymbol{r}, \boldsymbol{r}') \cdot \boldsymbol{a}_{n'} dS' \Big|_{\boldsymbol{r} \in S^+}] dS \end{aligned} \tag{7}$$

As illustrated in Figure 4, in HSMLFMM, the interactions can be divided into near and far interactions. The near interactions can be calculated by MoM. For far-field interactions, the half-space Green function is implemented. The half-space MLFMM's Green function can be written as:

$$\bar{\bar{\bar{G}}}_{Aii}(\boldsymbol{r}, \boldsymbol{r}') = \bar{\bar{I}} \frac{e^{-jk_i|\boldsymbol{r}-\boldsymbol{r}'|}}{4\pi|\boldsymbol{r}-\boldsymbol{r}'|} - (\bar{\bar{I}} - 2\hat{z}\hat{z}) \frac{e^{-jk_i|\boldsymbol{r}-\boldsymbol{r}_I'|}}{4\pi|\boldsymbol{r}-\boldsymbol{r}_I'|} \tag{8}$$

where $\boldsymbol{r}$ represents the target point and $\boldsymbol{r}'$ and $\boldsymbol{r}_I'$ represent the source point and image source point, respectively. We set $z = 0$ as the ground plane. The first term on the right-hand side represents the direct field contribution from the source, while the second term represents the reflected field contribution from the image source. In the image term, the reflection coefficient matrix $-(\bar{\bar{I}} - 2\hat{z}\hat{z})$ corresponds to a PEC ground assumption, which serves as the kernel of the half-space Green function in the spectral domain. Equation (8) consists of the upper half-space Green function and the image term accounting for ground reflections. Interactions of the source group and target group can be decomposed into aggregation, translation, and disaggregation steps. In this paper, we set $\gamma = 1$, which corresponds to using only the EFIE formulation. This choice is appropriate for the perfectly conducting obstacle surfaces considered in our ILS multipath interference scenarios, as EFIE provides accurate and stable solutions for PEC scatterers.

Regarding ground modeling, our simulations employ a lossy dielectric half-space with parameters representative of a concrete runway: relative permittivity $\varepsilon_r = 10$ and conductivity $\sigma = 0.01$ S/m. The HSMLFMM formulation rigorously accounts for the infinite lower half-space through the Sommerfeld integral in the half-space Green function, allowing arbitrary dielectric parameters to be assigned to the ground with high accuracy. However, for finite-sized obstacles in the upper half-space (e.g., the hangar and metallic baffles), the integral equation formulation (EFIE/CFIE) used in this implementation is formulated for PEC surfaces only, as extending it to finite-sized dielectric objects would require a substantially different formulation. This is consistent with the standard HSMLFMM framework, where the half-space Green function handles the infinite ground interface while the surface-current solver handles the finite scatterers as PEC.

2.2.2. Genetic Algorithm

GA is a stochastic global optimization method that simulates natural selection and genetic mechanisms. It iteratively evolves a population of encoded solutions through operations such as selection, crossover, and mutation, gradually converging toward the optimal solution.

Our approach employs a floating-point encoded genetic algorithm to solve optimization problems, utilizing the "crossover + uniform mutation" operators.

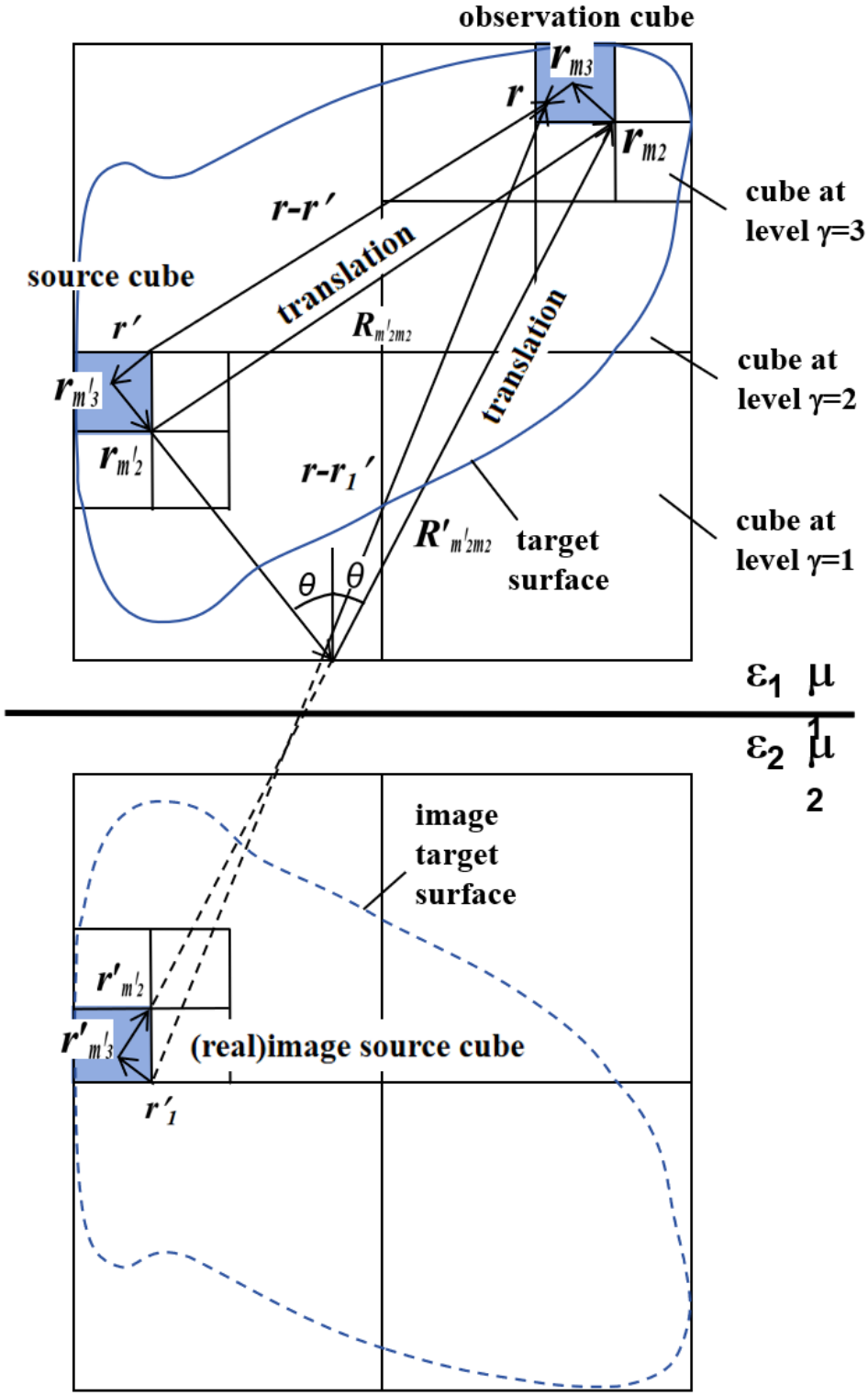


Figure 4. Multilevel clustering in 3D MLFMM and generalization to a half-space environment using real images to account for far interface interactions.

The algorithmic process is as follows:

1. Randomly generate the initial population (F_0).
2. Evaluate the fitness of each individual (chromosome) using the fitness function.
3. Sort the fitness values in ascending order and select the top parent number individuals to form the parent population (F_1).

4. Randomly select parents from F_1 to perform chromosome crossover, generating offspring (population F_2).
5. Merge populations ($F_1 + F_2$) for mutation.
6. Screen the merged population and evaluate fitness for each individual.
7. Check termination criteria (e.g., maximum generations reached or fitness threshold met). If satisfied, output the optimal solution; otherwise, return to Step 3.

The algorithm flow is shown in Figure 5.

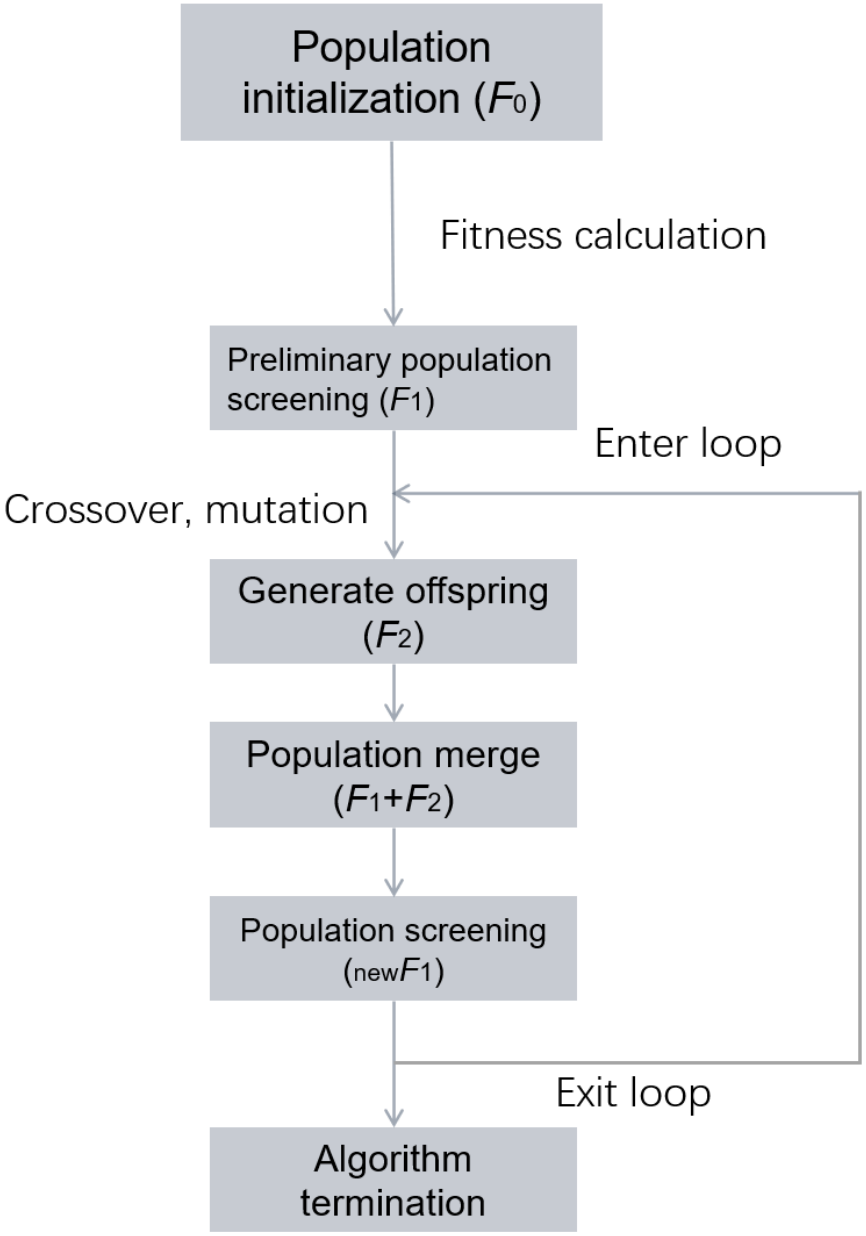


Figure 5. Genetic algorithm flowchart.

In the algorithm, the core elements are as follows:

Population Initialization

Generate an initial population of size N using a uniform random distribution within the feasible region. Independently generate $N \times D$ real numbers between 0 and 1 (where D is the number of genes), forming an initial population matrix encoded as real numbers.

This ensures the initial solutions uniformly cover the entire search space. The relationship is shown in the following formula:

$$\mathbf{P}^{(0)} \in \mathbb{R}^{N\times D}, \quad P_{ij}^{(0)} \sim \mathcal{U}(0,1), \quad i = 1\ldots N, j = 1\ldots D \tag{9}$$

In this formulation, $\mathbf{P}^{(0)}$ represents the initial population matrix, where the superscript (0) denotes the initial generation. Each element $P_{ij}^{(0)}$ corresponds to the initial gene value of the j-th variable (dimension) of the i-th individual in the population. The symbol $\mathcal{U}(0,1)$ indicates that every element is independently sampled from a uniform random distribution between 0 and 1. This initialization method ensures that the population is uniformly scattered across the feasible search space, providing a diverse starting point for subsequent evolutionary operations.

Fitness Function Design

The purpose of the fitness function is to calculate the fitness value of each individual within a given population. It evaluates an individual's performance within the problem domain based on its characteristics.

In this scheme, fitness is defined as the maximum absolute value of the difference in depth of modulation (DDM) across all observation points, where a smaller value indicates better performance. The DDM is calculated as twice the ratio of SBO to CSB electric field amplitudes multiplied by the cosine of their phase difference, as defined in Equation (1).

The formula for calculating fitness is as follows.

The ratio for the i-th sample point is calculated as:

$$\text{ratio}_i = 2 \cdot \frac{|E_{\text{sbo},i}|}{|E_{\text{csb},i}|} \cdot \cos(\phi_{\text{sbo},i} - \phi_{\text{csb},i}) \tag{10}$$

The final fitness is:

$$f = \max_{i=1}^{N} |\text{ratio}_i| \tag{11}$$

where N is the number of samples. The field components E_{sbo}, E_{csb}, ϕ_{sbo}, and ϕ_{csb} follow the definitions established in Section 2.1.

Genetic Operators

- Selection: The algorithm employs cumulative probability selection to choose parental genes for the population. This method selects parent individuals based on the proportion of their fitness values, with higher-fitness individuals having a greater chance of being selected as parents for the next generation.
- Crossover: The crossover operation (also known as hybridization) involves exchanging and recombining gene segments from two or more individuals within a genetic algorithm, thereby generating new offspring that carry the advantages of both parents. This process opens up new regions within the solution space, seeking more optimal possibilities.
  Common crossover methods include single-point crossover, multi-point crossover, and uniform crossover.
  This scheme employs single-point crossover, the principle of which is illustrated in Figure 6.
- Mutation: Uniform mutation is employed, where selected individuals undergo random selection with probability. Each dimension is regenerated uniformly at random within its interval, preserving population diversity and preventing premature convergence.

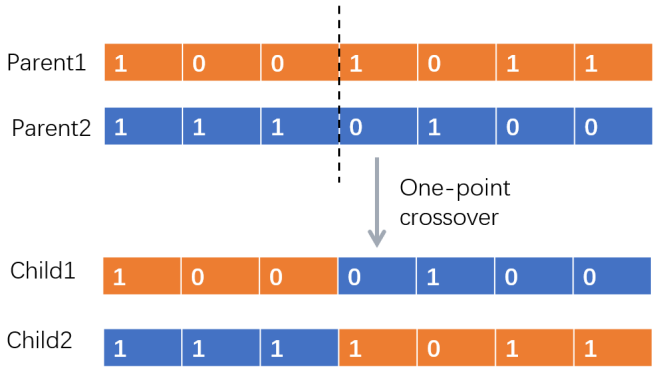


Figure 6. One-point crossover diagram.

The mutation principle is illustrated in Figure 7.

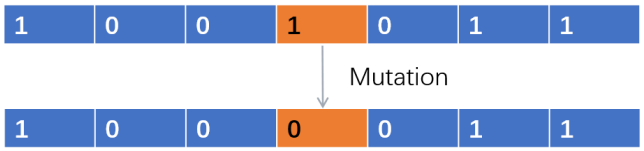


Figure 7. Schematic diagram of the mutation operator.

Our approach employs a GA to modify building shapes, achieving a "stealth" effect for airport structures. MLFMM simulations are used to validate the DDM of each GA seed (i.e., each design proposal), with the optimal seed selected as the final design solution.

3. Experimental Results

The methodology of our approach is outlined as follows:

- Initialization: Randomly generate the first generation of seeds, where each seed represents a design scheme for adding metal plates adjacent to the building. The specific parameters include the coordinates, length, and height of each metal plate.
- Fitness evaluation: Submit each seed to HSMLFMM simulation to compute the maximum absolute DDM along the glide path for each individual, which serves as the fitness value.
- Termination check: Determine whether the termination condition (maximum generation or convergence criterion) is met. If satisfied, output the optimal metal plate layout.
- Selection: If not terminated, select parent individuals from the current population based on their fitness values.
- Crossover: Generate offspring by recombining the genes of parent individuals.
- Mutation: Perturb the genes of selected individuals with a given probability to maintain population diversity.
- New generation: Form the next generation by merging parents and offspring, then return to the fitness evaluation step.

This iterative process continues until the termination condition is met. The complete workflow is illustrated in Figure 8.

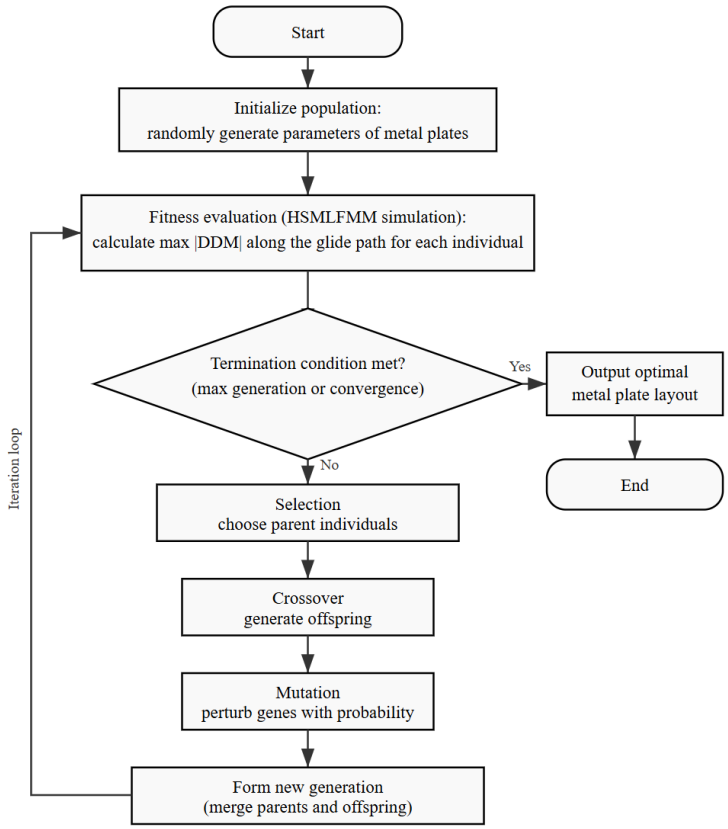


Figure 8. Closed-loop optimization workflow.

3.1. Experimental Procedure

In the ILS standard, the localizer is implemented using two log-periodic antennas. As shown in Figure 9, the two red arrows represent the antennas, and the yellow dashed line indicates the runway centerline. Both antennas have a height of 2.72 m and are placed on either side of the runway centerline, each at a lateral distance of 1.19 m. The frequency of the pilot signal is set to 110 MHz, and the mesh size for the MLFMM is set to 0.34 m.

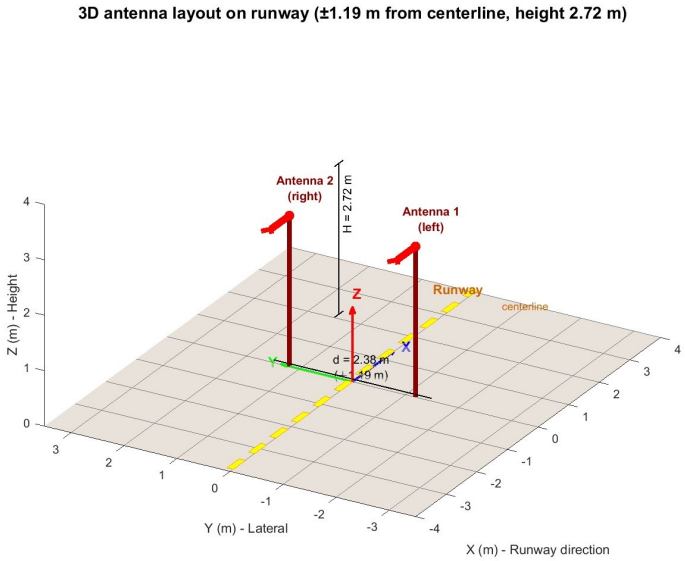


Figure 9. Three-dimensional antenna layout.

In our scheme, the receiver is placed on a 4 m high approach runway extending from 0 m to 4000 m. A 30 m long, 15 m high metallic plate—simulating a hangar—is located

500 m ahead of the antenna and 150 m laterally from the extended runway centerline, as shown in the top-view layout of Figure 10 (blue block). One to four additional metallic plates (red blocks in Figure 10) are then introduced beside the hangar, each positioned 150 m from the center line. Figure 10 illustrates the optimized simulation geometry for the 150 m lateral distance case.

The design variables for optimization include the number of additional plates, as well as the coordinates, length, and height of each plate. These parameters are encoded as chromosomes and optimized by the GA.

The performance of a GA is governed by several parameters: algorithmic variant (simple, multi-population, steady-state, etc.), termination criterion, crossover probability P_{cross}, mutation probability P_{mut}, and population size S_{pop}. In our experiments, a parametric investigation was conducted on S_{pop}, P_{cross}, and P_{mut}. The final configuration adopted is as follows: the population size is set to twice the chromosome length, the crossover probability is 50%, and the mutation probability is 12.5%.

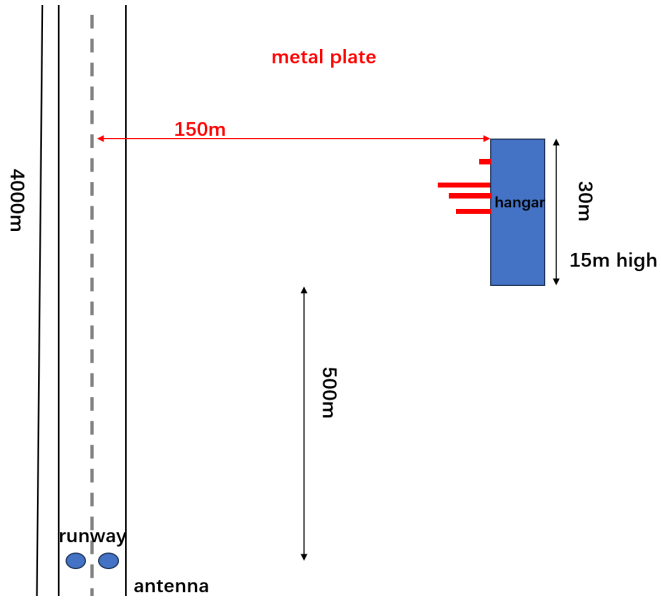


Figure 10. GA-based stealth building design schematic (metal plates at 150 m lateral distance).

3.2. Optimization Results for Different Lateral Distances

To systematically verify the adaptability and robustness of the proposed optimization scheme, supplementary control experiments were performed. In addition to the baseline lateral offset of 150 m, the metallic plates were repositioned at 50 m, 100 m, and 200 m from the runway centerline, allowing the scheme's performance under varying spatial layouts to be thoroughly assessed.

Figure 10 presents the top-view layout of the optimized simulation configuration for the 150 m lateral distance, as a representative example of the four tested offsets. The runway is located on the left side of the figure, with the localizer antenna placed on the runway centerline. The blue square indicates the hangar (30 m × 15 m metallic plate) positioned 150 m away from the runway centerline. The red rectangles represent the additional metallic baffles optimized by the GA, rearranged at the same lateral distance. This configuration is the outcome of multiple GA generations.

3.2.1. Case 1: Baseline Scenario (Lateral Distance 150 M)

Without adding metal plates (only perimeter hangar), the maximum absolute DDM value reached 49.9. After multiple generations of GA computation, it decreased to 4.63—a reduction of 90.5%—validating the effectiveness of this solution at typical distances. The

calculation results are shown in Figure 11 (blue origin indicates only metal perimeter walls; red GA indicates results after adding metal plates).

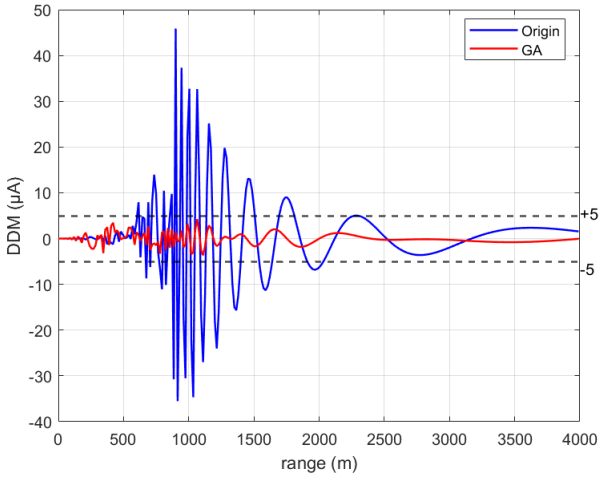


Figure 11. DDM comparison for 150 m case (without vs. with GA-optimized plates).

Figure 12 illustrates the GA convergence process for this scenario.

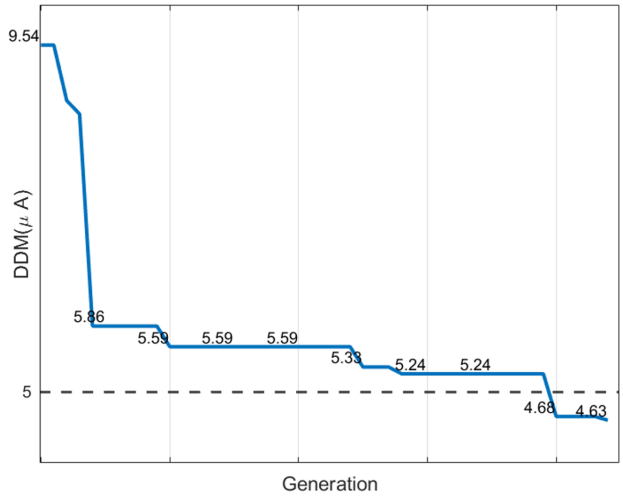


Figure 12. DDM iteration process for the 150 m case.

After GA computation, the final design scheme involves adding four metal plates, with the parameters shown in Table 1.

Table 1. GA-optimized metal-plate design (150 m).

Plate	Initial Point (m)	Height (m)	Width (m)
1	516	15	15.5
2	519	8.5	18
3	525.5	4	1
4	515.5	2.5	10.5

3.2.2. Case 2: 50 M Lateral Distance Scenario

To evaluate optimization capabilities in close-range strong reflection environments, experiments were conducted with a lateral distance of 50 m between metal plates. In this scenario, the original DDM exhibited a high peak value. Following GA optimization,

significant suppression effects were still achieved, with the optimal DDM being reduced to 4.49.

Figure 13 illustrates the channel layout schematic for the 50 m scenario.

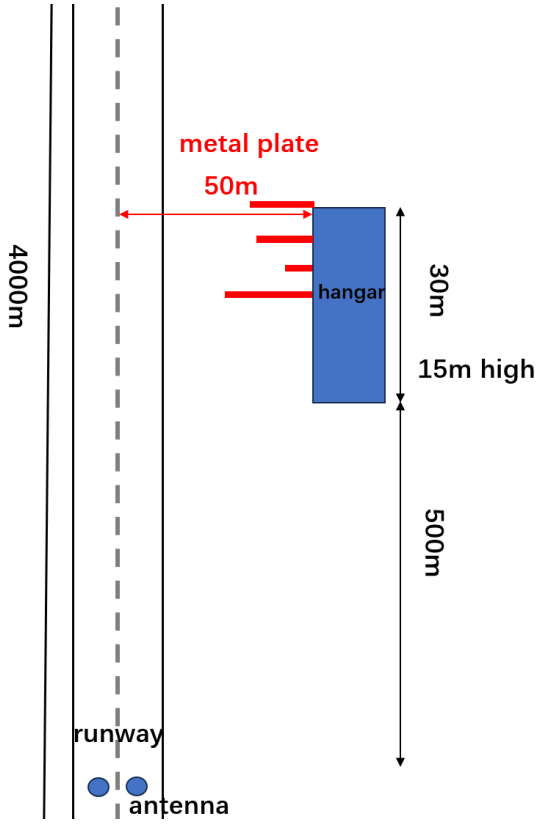


Figure 13. Schematic diagram of metal plates positioned 50 m from the runway centerline.

Figure 14 shows the convergence curve of the DDM over generations during the GA iteration process in this scenario.

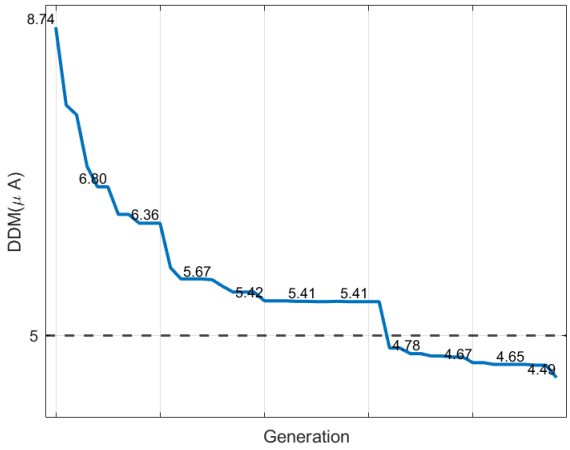


Figure 14. DDM iteration process for the 50 m case.

Figure 15 shows a comparison of the distribution of DDM along the heading before and after optimization, where the blue origin indicates only metal perimeter walls and the red GA indicates results after adding metal plates.

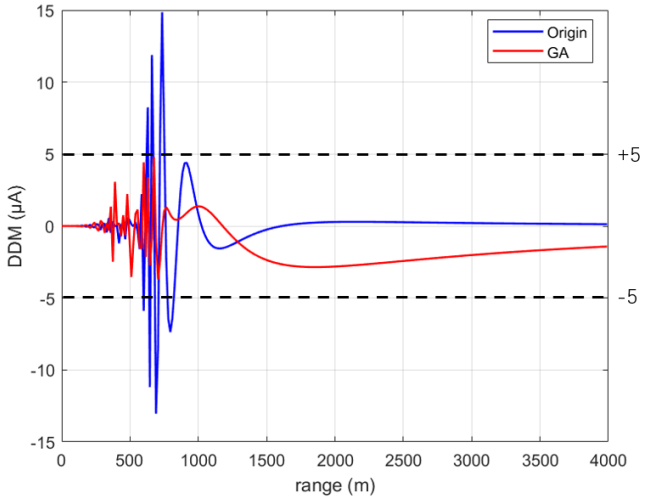


Figure 15. DDM comparison for 50 m case (without vs. with GA-optimized plates).

The final design scheme of the metal plates is shown in Table 2.

Table 2. GA-optimized metal-plate design (50 m).

Plate	Initial Point (m)	Height (m)	Width (m)
1	520.5	11	15.5
2	531	12.5	12
3	540	5	15.5
4	512	10	18

3.2.3. Case 3: 100 M Lateral Distance Scenario

At a distance of 100 m, the reflected intensity was relatively moderate. After GA optimization, the DDM decreased to 4.78, indicating that this scheme still achieved excellent optimization performance at medium distances.

Figure 16 shows the layout schematic for the 100 m scenario.

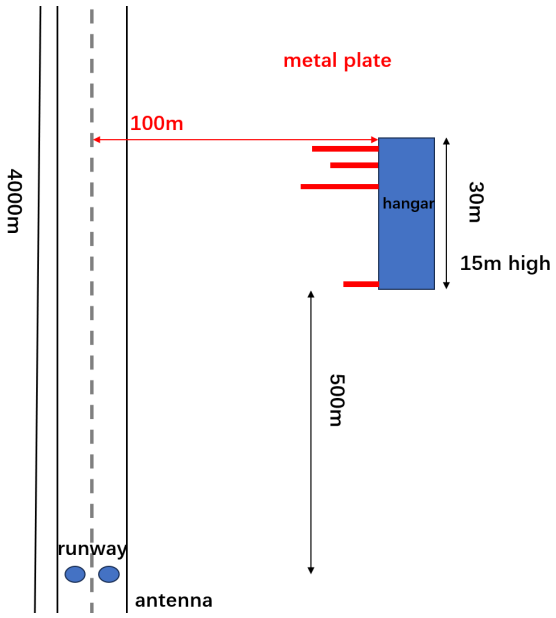


Figure 16. Schematic diagram of metal plates positioned 100 m from the runway centerline.

Figure 17 illustrates the convergence process of the GA in this scenario.

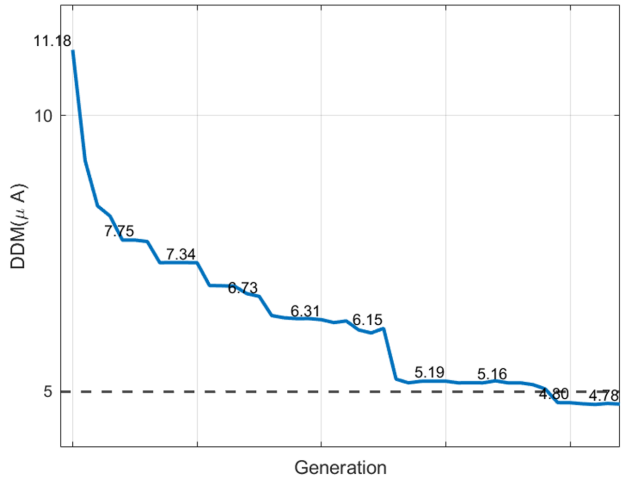


Figure 17. DDM iteration process for the 100 m case.

Figure 18 shows a comparison of the optimization results. After implementing the proposed solution, the maximum DDM value remains low while the average DDM value decreases significantly.

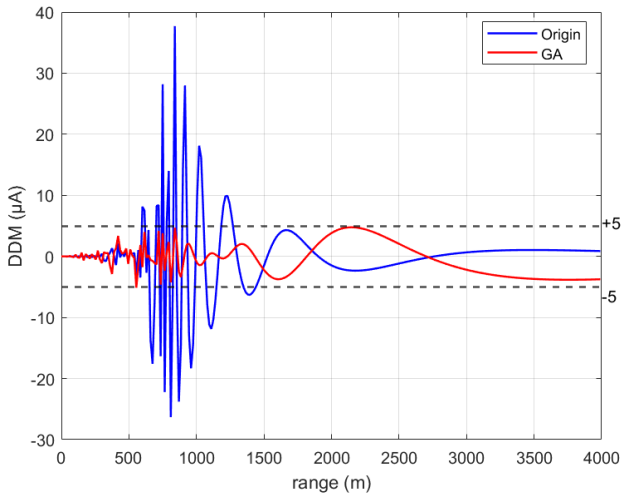


Figure 18. DDM comparison for 100 m case (without vs. with GA-optimized plates).

The final design scheme of the metal plates is shown in Table 3.

Table 3. GA-optimized metal-plate design (100 m).

Plate	Initial Point (m)	Height (m)	Width (m)
1	521	14.5	16.5
2	525.5	14.5	13.5
3	500	6	11.5
4	517.5	10.5	18

3.2.4. Case 4: 200 M Lateral Distance Scenario

At a 200 m distance, the optimized DDM reached 4.87, further demonstrating the applicability of this solution across different spatial scales.

Figure 19 shows the layout schematic for the 200 m scenario.

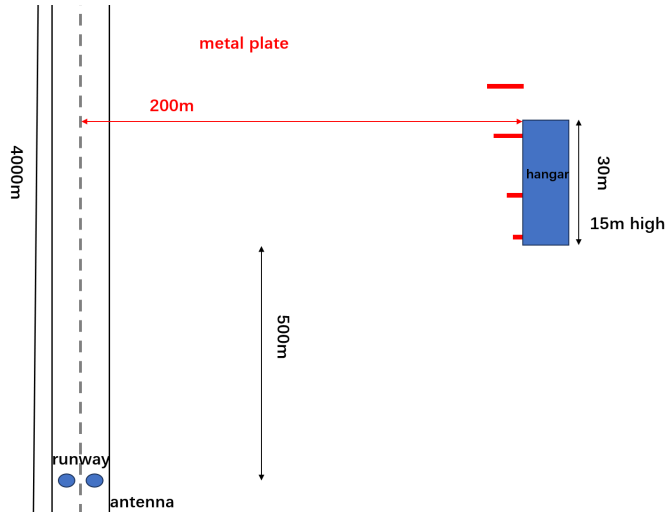


Figure 19. Schematic diagram of metal plates positioned 200 m from the runway centerline.

Figure 20 illustrates the convergence process of the GA in this scenario.

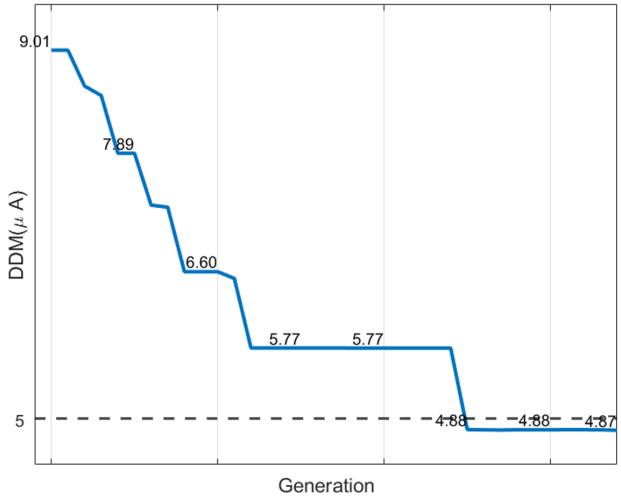


Figure 20. DDM iteration process for the 200 m case.

Figure 21 shows a comparison of the DDM distribution before and after optimization.

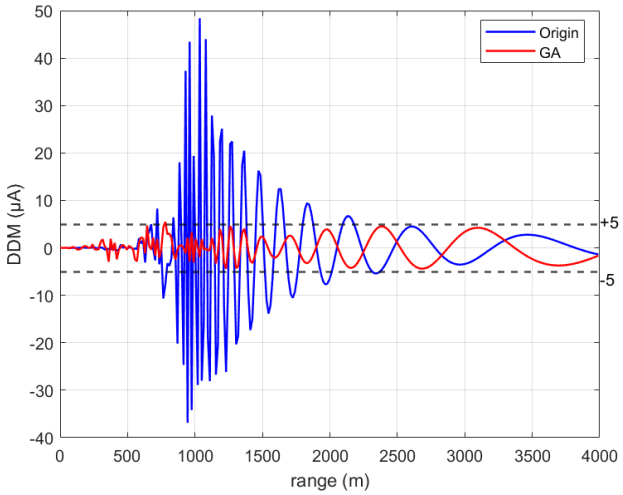


Figure 21. DDM comparison for 200 m case (without vs. with GA-optimized plates).

The final design scheme of the metal plates is shown in Table 4.

Table 4. GA-optimized metal-plate design (200 m).

Plate	Initial Point (m)	Height (m)	Width (m)
1	504.5	10	1
2	547.5	13	9
3	513	14.5	3.5
4	527	14	6.5

3.2.5. Comprehensive Comparative Analysis

To more intuitively demonstrate the stability of optimization effects at different distances, Figure 22 presents a comprehensive comparison across four lateral distance scenarios. As shown in Figure 22a, the peak DDM is significantly reduced after GA optimization in all cases. Figure 22b further shows the corresponding reduction percentages, ranging from 75.85% to 90.73%, with a maximum of 90.73% achieved at 150 m. Figure 22c displays the optimized DDM values, all of which fall below the ICAO Annex 10 tolerance limit of 5 μA (indicated by the horizontal dashed line), confirming compliance with international standards for CAT III operations. These results demonstrate that regardless of the metal plate's distance from the runway centerline, GA optimization consistently achieves significant suppression effects, validating the robust performance and engineering feasibility of the proposed solution.

Before concluding this section, it is worth discussing the modeling simplification adopted in this study. The hangar is represented as a flat PEC plate (30 m × 15 m). This simplification is justified by the fact that, for ILS signals at 110 MHz, the dominant scattering contribution comes from the large planar facade facing the runway, while the roof, side walls, and internal structural beams contribute only second-order effects—particularly given that the antenna height (2.72 m) is lower than the building height (15 m). To validate this approximation, we compared the flat-plate model with a more realistic 3D hangar model; the DDM difference was only 3.4% (50.40 vs. 48.72), confirming that the simplification introduces negligible error and that the optimized baffle layouts obtained from the simplified model are robust for real hangar geometries.

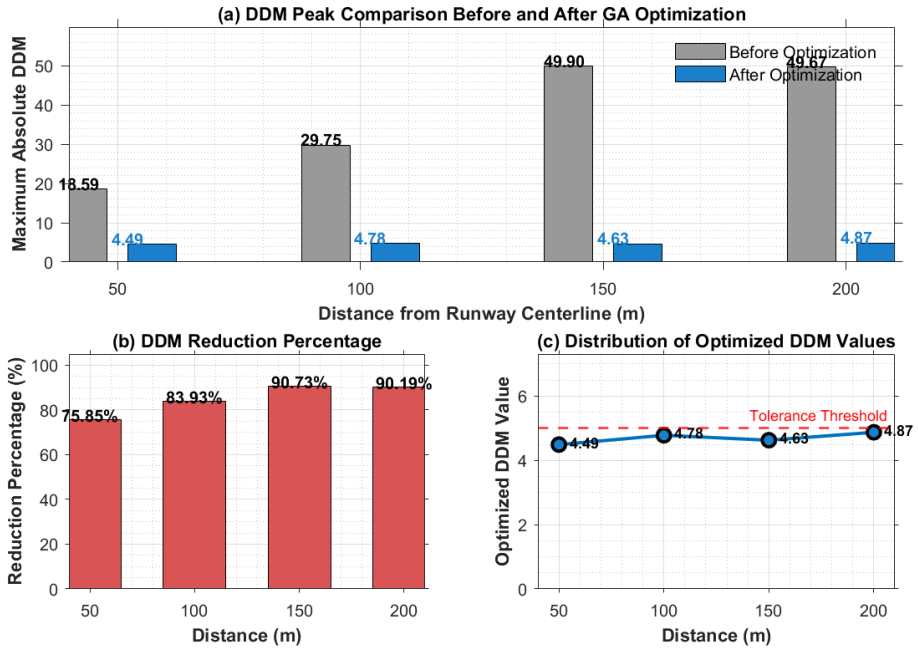


Figure 22. Comprehensive performance comparison of GA optimization across different lateral distances.

4. Conclusions

This paper addresses the multipath interference problem in ILS localizer signals caused by airport structures by proposing and validating a genetic algorithm (GA) optimization design methodology that directly targets the minimization of the key guidance parameter, DDM. The method transforms the empirically driven "stealth building" design into an automated mathematical optimization problem. By genetically encoding the layout parameters of metallic baffles and employing the high-fidelity half-space MLFMM for rapid electromagnetic performance evaluation, an efficient "generate-and-evaluate" optimization loop is established.

Simulation experiments demonstrate that the GA optimization framework exhibits robust search capability and reliability across interference scenarios at various distances. The optimized metallic baffle layouts generate specific scattering fields that destructively interfere with the original interfering field, effectively suppressing both the peak value and the distribution of DDM within the critical approach glide path to levels within the tolerance limits, achieving a maximum reduction exceeding 90%. This confirms the feasibility of proactively correcting the composite radiation pattern by intentionally introducing and optimizing secondary scatterers to protect the core navigation parameter.

The primary contributions of this work are twofold. First, it achieves a direct alignment of the optimization objective from intermediate electromagnetic quantities to the final system performance metric (DDM), making the design more pertinent to engineering outcomes. Second, it provides a generalizable and automated design workflow adaptable to specific obstacle configurations at different airports, reducing the reliance on expert experience inherent in traditional methods. Future work may expand the optimization variables to include a wider range of materials and structures and further investigate the application potential of this technique in complex, multi-obstacle environments and dynamic scenarios. In particular, we plan to incorporate a hybrid ray-tracing (RT) and finite-difference time-domain (FDTD) method to enable real-time re-optimization under dynamic scattering conditions—such as those caused by taxiing aircraft or moving ground vehicles. It is also worth noting that the current framework is not limited to flat-ground assumptions; complex terrain profiles can be readily accommodated within the existing formulation by properly defining the half-space parameters. These extensions would significantly broaden the applicability of the proposed method toward practical airport deployment.

Author Contributions: Conceptualization, Z.L. (Zihao Li); methodology, Z.L. (Zihao Li), J.L. and L.Z. (Lixiang Zuo); software, Z.L. (Zihao Li); validation, Z.L. (Zihao Li) and J.L.; formal analysis, J.L.; investigation, Z.L. (Zexin Lin); data curation, Z.L. (Zexin Lin); writing—original draft preparation, Z.L. (Zihao Li), J.L. and Z.L. (Zexin Lin); writing—review and editing, L.Z. (Lixiang Zuo), M.W. and L.Z. (Liyun Zuo); visualization, J.L.; supervision, L.Z. (Liyun Zuo); project administration, L.Z. (Liyun Zuo); funding acquisition, L.Z. (Liyun Zuo). All authors have read and agreed to the published version of the manuscript.

Funding: This research was funded by the Research Fund of the Department of Education of Guangdong Province, grant number 2024KQNCX248; the Guangdong Basic and Applied Basic Research Foundation, China, grant number 2024A1515010144; the Special Fund for Scientific and Technological Innovation Strategy of Guangdong Province (College Student Scientific and Technological Innovation Cultivation "Climbing Program"), grant number pdjh2025bk325; and the High-level Talents of Guangdong Polytechnic Startup Project, grant number XJGCC202406.

Data Availability Statement: The original contributions presented in this study are included in the article. Further inquiries can be directed to the corresponding author.

Acknowledgments: The authors would like to thank the CAAC Middle South Regional Air Traffic Management Bureau for providing theoretical guidance on ILS and computational server support for this work.

Conflicts of Interest: The authors declare no conflicts of interest. The funders had no role in the design of the study; in the collection, analyses, or interpretation of data; in the writing of the manuscript; or in the decision to publish the results.

References

1. Geise, R.; Enders, A.; Vahle, H.; Spieker, H. Scaled Measurements of Instrument-Landing-System Disturbances Due to Large Taxiing Aircraft. *IEEE Trans. Electromagn. Compat.* **2008**, *50*, 485–490. [CrossRef]
2. Thain, A.; Estienne, J.P.; Robert, J.; Peres, G.; Cambon, G.; Evain, L.; Spitz, B. A solution for ILS disturbance due to a building. In Proceedings of the 2012 6th European Conference on Antennas and Propagation (EUCAP), Prague, Czech Republic, 26–30 March 2012; pp. 2392–2395.
3. Thain, A.; Estienne, J.P.; Robert, J.; Platon, Y.; Herve, A.; Piche, A. Stealth Buildings at Airbus Group Innovations: Low-cost solutions to radio perturbations. *IEEE Antennas Propag. Mag.* **2016**, *58*, 16–27. [CrossRef]
4. Zhao, Y.; Wang, Q.; Fu, J.; Zhang, Q.; Feng, H.; Wu, Q. New Synthesis Method for Broadband Multilayer Absorber Using Multi-Objective Genetic Algorithm. *IEEE Photonics Technol. Lett.* **2022**, *34*, 1265–1268. [CrossRef]
5. Xing, Z.; Lv, Z.; Wang, X.; Guo, C.; Gou, Y.; Wang, L. Ultrathin Low-RCS Circularly Polarized Antenna Using 2-Bit Hybrid Metasurface Optimized by Genetic Algorithm. *IEEE Antennas Wirel. Propag. Lett.* **2026**, *25*, 29–33. [CrossRef]
6. Ren, Z.; Liu, Y.-Q.; Wang, Y.; Lu, L.; Qi, K.; Yin, H. Ultra-Broadband RCS Reduction Based on Optimized Coding "Whale-Shaped" Polarization Conversion Metasurface with Angular Stability. *IEEE Access* **2022**, *10*, 50479–50486. [CrossRef]
7. Corus, D.; Oliveto, P.S. Standard Steady State Genetic Algorithms Can Hillclimb Faster Than Mutation-Only Evolutionary Algorithms. *IEEE Trans. Evol. Comput.* **2018**, *22*, 720–732. [CrossRef]
8. Fan, Q.; Yan, X. Self-Adaptive Differential Evolution Algorithm With Zoning Evolution of Control Parameters and Adaptive Mutation Strategies. *IEEE Trans. Cybern.* **2016**, *46*, 219–232. [CrossRef] [PubMed]
9. Dholey, M.K.; Sinha, D. EEMR-PSO-CUCKOO: Energy Efficient MANET Routing Using Hybrid PSO and CUCKOO Search. *J. Mob. Multimed.* **2025**, *21*, 729–748.
10. Cheng, Y.-F.; Li, D.; Chen, S.; Wang, G. A Novel Wideband Decoupling Method Based on Even-Odd-Mode Analysis and Genetic Algorithm Optimization. *IEEE Antennas Wirel. Propag. Lett.* **2023**, *22*, 2507–2511. [CrossRef]
11. Wang, C.; Peng, L.; Ma, J.; Shi, B.; Zhu, Z.-b. Multiobjective Integrated Optimization Design of Lens Antenna Based on a Competition and Cooperation Model With Neural Network and Evolutionary Algorithm. *IEEE Antennas Wirel. Propag. Lett.* **2024**, *23*, 4698–4702. [CrossRef]
12. Gao, T.-Y.; Jiao, Y.-C.; Zhang, Y.-X.; Zhang, L. A Hybrid Self-Adaptive Differential Evolution Algorithm With Simplified Bayesian Local Optimizer for Efficient Design of Antennas. *IEEE Trans. Antennas Propag.* **2025**, *73*, 391–404. [CrossRef]
13. Ha, T.D.; Nie, X.; Akinsolu, M.; Liu, B.; Chen, P.-Y. An Artificial-Intelligence-Assisted Optimization of Imperceptible Multimode Rectenna. *IEEE Antennas Wirel. Propag. Lett.* **2024**, *23*, 3559–3563. [CrossRef]
14. Wan, S.; He, B.; Lu, P.; Guan, X.; Zhang, X. A Uniplanar, Quasi-Isotropic Folded Dipole Design Based on Hybrid GA-PSO Optimization. *IEEE Antennas Wirel. Propag. Lett.* **2025**, *24*, 1158–1162. [CrossRef]
15. Bagherkhani, S.; Rahmat-Samii, Y.; De Flaviis, F. An Automated Dynamic Solution-Space Adaptation in Particle Swarm Optimization. *IEEE Trans. Antennas Propag.* **2025**, *73*, 9523–9528. [CrossRef]
16. Geng, N.; Sullivan, A.; Carin, L. Multilevel fast-multipole algorithm for scattering from conducting targets above or embedded in a lossy half space. *IEEE Trans. Geosci. Remote Sens.* **2000**, *38*, 1561–1573. [CrossRef]
17. Honda, J. Influence of Scattering Order on ILS Localizer Using Ray-Tracing Method. In Proceedings of the 2023 IEEE International Symposium on Antennas and Propagation (ISAP), Kuala Lumpur, Malaysia, 30 October–2 November 2023; pp. 1–2. [CrossRef]
18. Thain, A.; Estienne, J.P.; Peres, G.; Spitz, B.; Evain, L. A rigorous simulator of ILS perturbations. In Proceedings of the Fourth European Conference on Antennas and Propagation, Barcelona, Spain, 12–16 April 2010.
19. Thain, A.; Estienne, J.P.; Peres, G.; Spitz, B.; Evain, L.; Kumar, M. Comparisons of different approaches for ILS simulation. In Proceedings of the Fourth European Conference on Antennas and Propagation, Barcelona, Spain, 12–16 April 2010.
20. Li, Z.; Tan, J.; Guo, Q.; Su, Z.; Long, Y. A Parallel CE-LOD-FDTD Model for Instrument Landing System Signal Disturbance Analyzing. *IEEE Trans. Antennas Propag.* **2019**, *67*, 2503–2512. [CrossRef]

Disclaimer/Publisher's Note: The statements, opinions and data contained in all publications are solely those of the individual author(s) and contributor(s) and not of MDPI and/or the editor(s). MDPI and/or the editor(s) disclaim responsibility for any injury to people or property resulting from any ideas, methods, instructions or products referred to in the content.